

# Mesoscopic sliding ferroelectricity enabled photovoltaic random access memory for material-level artificial vision system

Received: 5 January 2022

Accepted: 1 September 2022

Published online: 14 September 2022

 Check for updates

Yan Sun<sup>1,6</sup>, Shuting Xu<sup>1,6</sup>, Zheqi Xu<sup>1,6</sup>, Jiamin Tian<sup>2</sup>, Mengmeng Bai<sup>1</sup>, Zhiying Qi<sup>1</sup>, Yue Niu<sup>1</sup>, Hein Htet Aung<sup>1</sup>, Xiaolu Xiong<sup>1</sup>, Junfeng Han<sup>1</sup>, Cuicui Lu<sup>1</sup>, Jianbo Yin<sup>3</sup>, Sheng Wang<sup>2</sup>, Qing Chen<sup>2</sup>, Reshef Tenne<sup>4</sup>, Alla Zak<sup>5</sup>✉ & Yao Guo<sup>1</sup>✉

Intelligent materials with adaptive response to external stimulation lay foundation to integrate functional systems at the material level. Here, with experimental observation and numerical simulation, we report a delicate nano-electro-mechanical-opto-system naturally embedded in individual multiwall tungsten disulfide nanotubes, which generates a distinct form of in-plane van der Waals sliding ferroelectricity from the unique combination of superlubricity and piezoelectricity. The sliding ferroelectricity enables programmable photovoltaic effect using the multiwall tungsten disulfide nanotube as photovoltaic random-access memory. A complete “four-in-one” artificial vision system that synchronously achieves full functions of detecting, processing, memorizing, and powering is integrated into the nanotube devices. Both labeled supervised learning and unlabeled reinforcement learning algorithms are executable in the artificial vision system to achieve self-driven image recognition. This work provides a distinct strategy to create ferroelectricity in van der Waals materials, and demonstrates how intelligent materials can push electronic system integration at the material level.

Since the demonstration of integrated circuits in the 1950s, the integration level of electronic systems has been remarkably developed and renovated<sup>1</sup>. On one hand, the success of Moore’s law enables the integration of billions of solid-state devices into a single die<sup>2</sup>, on the other, multiple functional submodules can be integrated into one chip or package, known as system on chip or system in package<sup>3,4</sup>. A typical functional system includes the sensing or input/output module for external information exchange, the processing module to execute the commands, the memory module to store the commands and data, and the power module to support the energy consumption<sup>5</sup>. Given the potential physical limit of Moore’s law, high-level system integration technology has drawn unprecedented attention. Non-von Neumann

architecture, which is inspired by neuromorphic computing and collocates the memory and process modules, is promising to reduce data traffic, time delay, and energy cost<sup>6,7</sup>. Comparably, in-sensor computing integrates sensing and processing modules, and the sense and process can operate synchronously with an ultrafast speed in edge applications<sup>8–10</sup>. Further on, floating-gate devices based on two-dimensional materials with functions of sensing, memory, and processing enabled by photon-induced trap charge release were demonstrated, and the construction of an artificial retinomorphic hardware system for motion detection was proposed<sup>11,12</sup>. With the explosive growth of data in the post Moore era, there is a great expectation for high-level system integration to further boost artificial intelligence and

<sup>1</sup>Beijing Institute of Technology, Haidian, Beijing 100081, China. <sup>2</sup>Department of Electronics, Peking University, Haidian, Beijing 100871, China. <sup>3</sup>Beijing Graphene Institute, Beijing 100095, China. <sup>4</sup>Department of Molecular Chemistry and Materials Science, Weizmann Institute of Science, Rehovot 760001, Israel. <sup>5</sup>Faculty of Sciences, Holon Institute of Technology, 52 Golomb St., Holon 5810201, Israel. <sup>6</sup>These authors contributed equally: Yan Sun, Shuting Xu, Zheqi Xu. ✉e-mail: [alzak@hit.ac.il](mailto:alzak@hit.ac.il); [yaoguo@bit.edu.cn](mailto:yaoguo@bit.edu.cn)

the internet-of-things. Herein a conceptual question is: which level can the system integration ultimately achieve?

From the perspective of material science, intelligent materials with controllable physical properties and reconfigurable responses to external stimuli are appropriate candidates to build functional electronic systems<sup>13</sup>. Ferroelectricity, which generates reversible spontaneous electric polarization with external voltage bias, is among the most preferred strategies to achieve memory in electronic devices<sup>14–20</sup>. Traditional ferroelectricity of both bulk and low-dimensional materials is generally regarded as the result of atomic position switching between the bi-stable states of the atomic unit cell structure<sup>14–16</sup>. The recently revealed parallelly stacked bilayer graphene or bilayer h-BN structures switching between AB and BA configuration was found to generate an interfacial out-of-plane spontaneous polarization<sup>21–25</sup>. Upon the centennial anniversary of ferroelectricity's discovery<sup>15–17</sup>, it is of great significance to explore new forms of ferroelectricity, and fully play their memory function to meet the current challenges of electronics for the artificial intelligence era.

In this research, we report a mesoscopic in-plane sliding ferroelectricity that results from the superlubricity of the van der Waals interface<sup>26–29</sup> and the piezoelectric nature of asymmetric structure of the WS<sub>2</sub> nanotube<sup>30–32</sup>. This ferroelectricity is different from traditional ferroelectricity that originates from atomic lattice switching discovered 100 years ago, as well as the recently revealed interfacial ferroelectricity of parallelly stacked bilayer graphene or h-BN<sup>14–17,21–25</sup>. The mesoscopic sliding ferroelectricity produces programmable and nonvolatile photovoltaic effect in WS<sub>2</sub> nanotubes, which are ideally suitable as photovoltaic random-access memory (PV-RAM). We further demonstrate a complete artificial vision system integrated in the 'smart' PV-RAM array, which enables synchronous multi-functions of sense, memory, compute, and power. Both labeled supervised learning and label-free reinforced learning are implantable in the PV-RAM

system, which is self-driven and spontaneously outputs robust electrical signals with recognized image patterns.

## Results

High-quality multiwall WS<sub>2</sub> nanotubes were synthesized and the devices were fabricated, as shown in Fig. 1a and Supplementary Fig. 1. The spontaneous photovoltaic effect of WS<sub>2</sub> nanotubes has been revealed in a previous report<sup>33</sup>, which is well reproduced in Fig. 1b and Supplementary Fig. 2. The photo absorption and photoelectrical response of WS<sub>2</sub> nanotube cover the nearly full red to blue visible band, which makes WS<sub>2</sub> nanotube suitable candidate to build the bottom devices for artificial vision systems, as shown in Supplementary Fig. 3 to Supplementary Fig. 8. The linearity of the photoresponse is evaluated in Supplementary Figs. 9 and 10. More interestingly, we discover that the photovoltaic effect of the WS<sub>2</sub> nanotubes is programmable. As shown in the upper Fig. 1c, initially, the photovoltage of a WS<sub>2</sub> nanotube device is 0.21 V and the photocurrent is  $-15.7$  nA. By applying various negative voltages bias of  $-3$  V,  $-4$  V, and  $-5$  V for 5 s prior to the  $I$ - $V$  tests, the  $I$ - $V$  curves shift and the photovoltage steps down to  $-0.07$  V,  $-0.34$  V, and  $-0.53$  V, and the photocurrent increases to  $6.0$  nA,  $14.3$  nA, and  $19.1$  nA, respectively. The direction of the photovoltaic effect is reversed. Further on, the photovoltage and photocurrent can be reversed back by applying positive voltage. As shown in the lower Fig. 1c, by applying voltage bias of  $3$  V,  $4$  V, and  $5$  V to the same device, the photovoltage step from  $-0.49$  V to  $-0.07$  V,  $0.14$  V, and  $0.17$  V, and the photocurrent decrease from  $18.6$  nA to  $5.3$  nA,  $-23.9$  nA, and  $-26.0$  nA, respectively. The linear plot of the  $I$ - $V$  curves is shown in Supplementary Fig. 11. Therefore, the photovoltaic effect of the WS<sub>2</sub> nanotube is adjustable with a prior bias, rather than having a fixed direction and magnitude. The reversion of the photovoltaic effect is reproducible and is obtained on multiple WS<sub>2</sub> nanotube devices, as shown in Supplementary Fig. 12. We also observe that there are devices

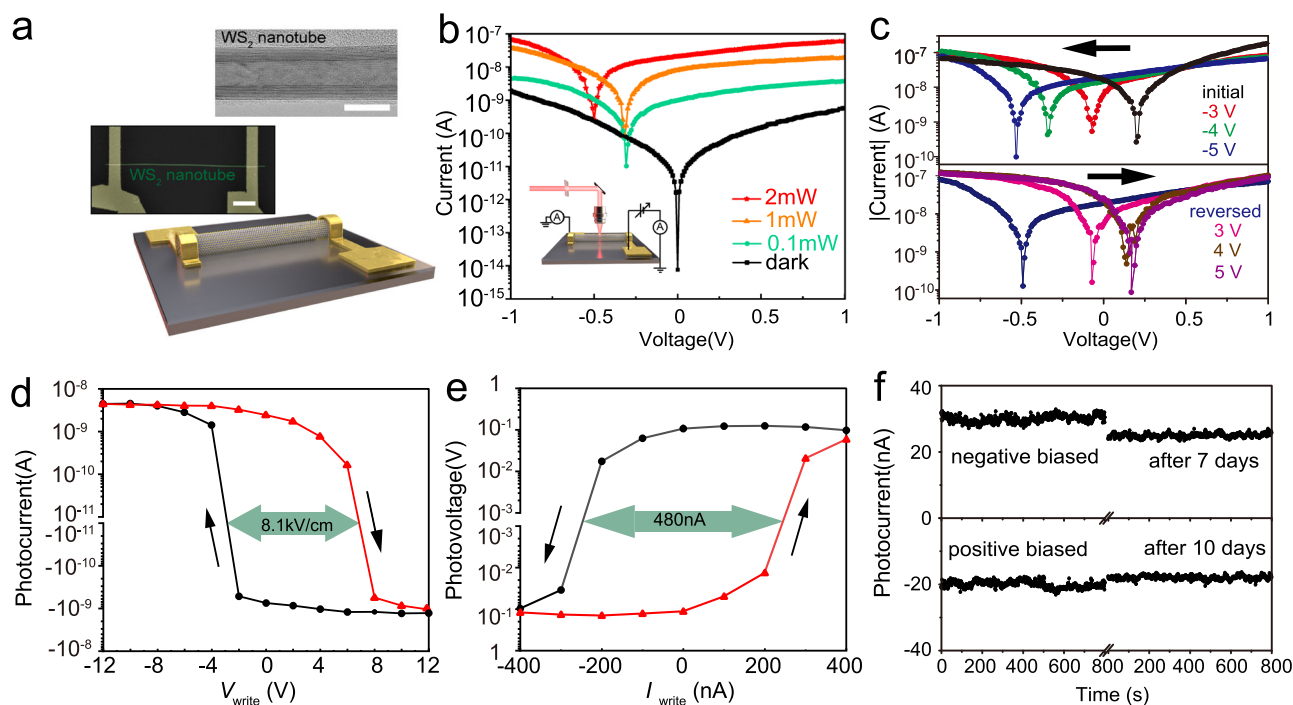


**Fig. 1 | Programmability of the photovoltaic effect in WS<sub>2</sub> nanotube.** **a** Upper: transmission electron microscopy image of a multiwall WS<sub>2</sub> nanotube, scale bar: 10 nm. Middle: scanning electron microscopy image (colored) of the WS<sub>2</sub> nanotube device, scale bar: 2  $\mu$ m. Lower: schematic of the WS<sub>2</sub> nanotube device. **b** Log scale  $I$ - $V$  curves with 633 nm laser spot focused at the middle of the channel with the power of 0 W, 0.1 mW, 1 mW, and 2 mW. Insert: Schematic diagram of the

photoresponse measurement. **c** Programmable photovoltaic effect in WS<sub>2</sub> nanotube with prior voltage bias of 0 V (initial),  $-3$  V,  $-4$  V,  $-5$  V (reversed),  $3$  V,  $4$  V, and  $5$  V, respectively, the black arrow indicates the test order. **d** Ferroelectric-like hysteresis loop of the photovoltaic effect through voltage sweep. **e** Ferroelectric-like hysteresis loop of the photovoltaic effect through current sweep. **f** Nonvolatility of the programmed photocurrent.

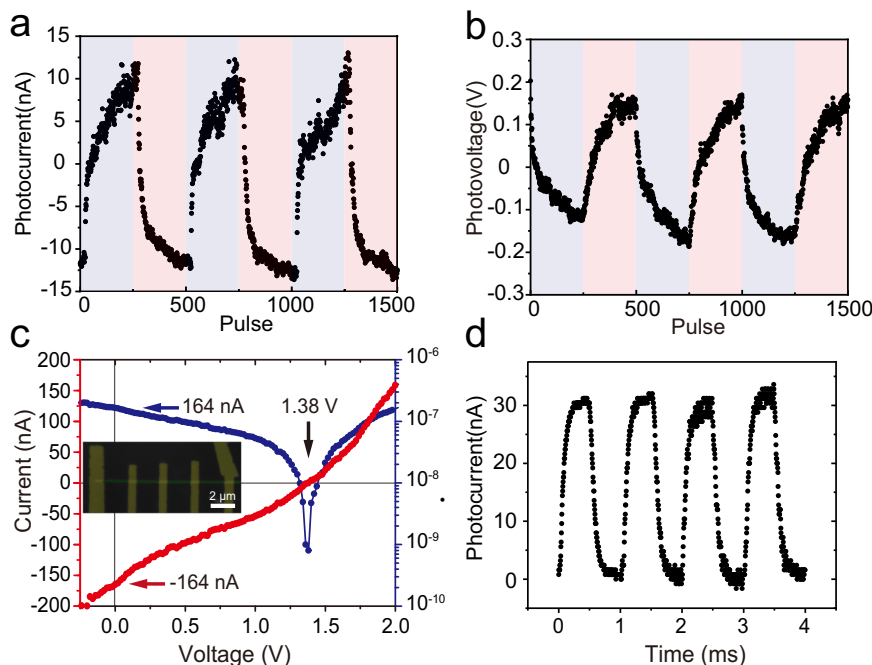


**Fig. 2 | Continuous programmability and additivity of the photovoltaic effect.** **a** Photocurrent programmed by voltage pulses. **b** Photovoltage programmed by

current pulses. **c**  $I$ - $V$  curve of the  $\text{WS}_2$  nanotube devices consisting of 4 series channels. **d** The photoresponse of the  $\text{WS}_2$  nanotube with 532 nm laser.

with indistinctive initial photovoltaic effect, still, the application of prior bias can generate the programmable photovoltaic effect. Besides the photovoltaic effect, the prior bias also alters the rectification behavior of the  $\text{WS}_2$  nanotube devices as shown in Supplementary Fig. 13, which indicates the change of the electrostatic status inside the nanotube, as we will discuss later in this article.

To further exhibit the programmability of the photovoltaic effect, we apply equidistant looping bias (as writing voltage  $V_{\text{write}}$ ) to the  $\text{WS}_2$  nanotube, and collect the corresponding photocurrent  $I_{\text{ph}}$  with zero bias ( $V_{\text{write}}$  retracted). As shown in Fig. 1d, the  $I_{\text{ph}}-V_{\text{write}}$  curve shows a ferroelectric-like hysteresis. The extracted coercivity is 9.8 V, or 8.1 kV/cm. Such a coercive electric field is relatively low compared to typical ferroelectric materials, which, for example, is around 40 kV/cm for  $\text{BiFeO}_3$  and  $\text{Pb}(\text{Zr}_{0.4}\text{Ti}_{0.6})\text{O}_3$ <sup>34–36</sup>. Similarly, the photovoltaic response can be also programmed with the current bias, as shown in Fig. 1e, the  $V_{\text{ph}}-I_{\text{write}}$  curve has a coercivity of 480 nA. The programmed photovoltaic effect is non-volatile and can be maintained for at least a few days, as shown in Fig. 1f.

We further show the programmability of the photovoltaic effect of  $\text{WS}_2$  nanotubes through the pulsed mode. As shown in Fig. 2a, by applying stimulating voltage pulses ( $\pm 6$  V, 5  $\mu\text{s}$ ) to the  $\text{WS}_2$  nanotube, the subsequent short circuit  $I_{\text{ph}}$  can be reversed and continuously modulated. The negative pulses increase  $I_{\text{ph}}$ , and the positive pulses decrease  $I_{\text{ph}}$ , and the direction of the  $I_{\text{ph}}$  can be reversed. The continuous programmability of the photovoltaic effect enables multilevel memories. Similarly, the photovoltaic effect can also be programmed with current pulses ( $\pm 500$  nA, 5  $\mu\text{s}$ ), as shown in Fig. 2b. The energy consumption to reverse the direction of the photovoltaic effect is estimated at a few hundred nJ (voltage  $\times$  current  $\times$  pulse width  $\times$  pulse number). The programmable photovoltaic response achieved by the compact two-terminal  $\text{WS}_2$  nanotube device is comparable to resistive random access memory (RRAM), magnetic random access memory (MRAM), or phase change random access memory (PCRAM)<sup>37–40</sup>. These three types of memories use different resistive, magnetic, or phase states to achieve non-volatile memory. Here,

we demonstrate the programmability of the photovoltaic effect of the  $\text{WS}_2$  nanotube device and describe it as a photovoltaic random access memory (PV-RAM). Compared to the fixed but unpredictable photovoltaic effect, the determinatively programmable photovoltaic effect with controlled sign or direction, allow photocurrent or photovoltage accumulation using  $\text{WS}_2$  nanotubes connected in parallel or in series. This demonstration is an important advance toward its practical application whether for energy harvesting or edge computing, as is shown in Supplementary Fig. 14. Given the intact length of the  $\text{WS}_2$  nanotube, the photovoltaic effect can also be multiplied by adding virtual electrodes to the channel<sup>41</sup>. As shown in Fig. 2c, the  $V_{\text{ph}}$  of the device with four series channels reach up to 1.38 V with a 10 mW laser illumination on the whole device area. The photoresponse of the  $\text{WS}_2$  nanotube with a chopped 532 nm laser is shown in Fig. 2d and Supplementary Fig. 15, from which we extracted the rise time of 64  $\mu\text{s}$  and fall time of 77  $\mu\text{s}$ . We list the photovoltaic performances of the  $\text{WS}_2$  nanotube device and a few low-dimensional material devices in previous studies, as is shown in Supplementary Table 1.

The PV-RAM, which has a programmable and non-volatile photovoltaic effect, lays the foundation for building a complete artificial vision system that achieves multi-functions of sense, memory, computing, and power. A 4 by 4 PV-RAM pixel array was fabricated on randomly dispersed  $\text{WS}_2$  nanotubes, as shown in Fig. 3a and Supplementary Fig. 16. Each pixel has a size of  $20 \times 20 \mu\text{m}^2$  and contains multiple  $\text{WS}_2$  nanotube channels. The PV-RAMs were connected in series to sum the photovoltages, and the output voltage  $V_{\text{ph}} = \Sigma(\mathbf{R}_{4 \times 4} * \mathbf{P}_{4 \times 4})$  performs a multiplication and sum operation (a convolution integral), with  $\mathbf{R}_{4 \times 4}$  being the photovoltage responsivity matrix that represents the weights,  $\mathbf{P}_{4 \times 4}$  being the photo intensity on each pixel as input. We note that there have been methods that massively fabricate carbon nanotube network devices<sup>42–44</sup>. Homogeneous  $\text{WS}_2$  nanotube networks can be obtained with further investigation into the synthesis, purification, dispersion, and fabrication processes. Here we focus on the photoelectrical behavior of the  $\text{WS}_2$  nanotube PV-

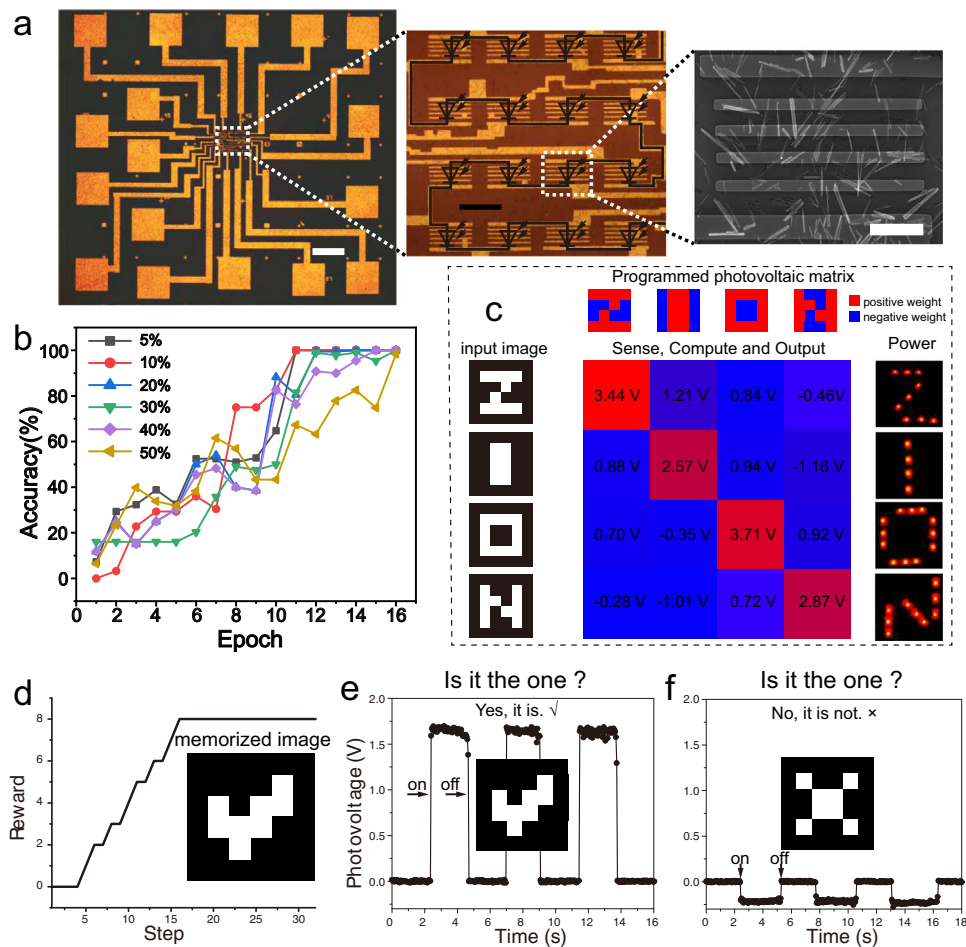


**Fig. 3 | Full-functional artificial vision system implanted in PV-RAM array.**

**a** Optical microscopy images (left and middle) and scanning electron microscopy image of the PV-RAM array. Scale bar, left: 100  $\mu\text{m}$ , middle: 20  $\mu\text{m}$ , right: 5  $\mu\text{m}$ . **b** Learning curve of accuracy with different levels of noise. **c** Demonstration of the artificial vision system. The binary weights were presented by the programmed

photoresponse. The input images of “Z”, “I”, “O”, “N” were projected onto the array by a 200 mW laser. The output voltages were collected, which indicates the probability. The output can flicker LED patterns through a capacitor. **d** The off-line reinforcement learning process. **e, f** Recognition of the learned image ( $\checkmark$ , **e**) from other image ( $\times$ , **f**).

RAM and prototype the integration of the artificial system into the PV-RAMs.

Firstly, we aim to achieve image identification of the letters ‘ZION’ with labeled training. We use off-line training with discrete binary and continuous weight, as shown in Fig. 3b, Supplementary Figs. 17 and 18. The trained weights are shown in Supplementary Figs. 19, 20. The PV-RAMs were then programmed according to the trained weight, and the image patterns were projected onto the array by a 532 nm laser through a customized pre-pattern mask. As shown in Fig. 3c, the WS<sub>2</sub> nanotube PV-RAM array, programmed following the binary weights, outputs a voltage that indicates the probability of the recognized pattern through a SoftMax function (see Supplementary Fig. 21). The magnitude of the output voltage of up to >2.5 V can further charge a capacitor (1  $\mu\text{F}$ ) and flicker LEDs fixed on office paper as flexible substrate (see Fig. 3c right, Supplementary Figs. 22 and 23). Therefore, the PV-RAM array can maintain the pre-set weight (memory), detect the light (sense), recognize the image pattern (compute), and spontaneously output a robust voltage that can drive secondary-level electronic devices (power). It is conceptually straightforward to further scale the pixels to larger dimensions or to multi-color, for example, Red-Green-Blue channels, as a future technological task.

Besides the labeled supervised learning, weights from unlabeled reinforced learning are also implantable in the PV-RAM array<sup>45</sup>. The training policy of the reinforced learning is to adjust the weight in the

neural network (photoresponse of each PV-RAM) to maximize the reward function, which is set  $Re = V_{\text{output}}^{\text{pattern}} - V_{\text{output}}^{\text{all}}/2$  in this case. Here  $V_{\text{output}}^{\text{pattern}}$  is the output voltage with the laser pattern projected on the array (a ‘ $\checkmark$ ’), and  $V_{\text{output}}^{\text{all}}$  is the output voltage with all PV-RAM in the array illustrated. Such a training strategy actually makes the PV-RAM array ‘remember’ the projected image. Figure 3d shows the learning curve of the reinforced learning. By programming the learned binary weight, the PV-RAM array can well recognize the previously memorized pattern (the ‘ $\checkmark$ ’) from random patterns (for example, a ‘ $\times$ ’), as shown in Fig. 3e, f, respectively.

Lastly, we discuss the mechanism for the programmability of the photovoltaic effect in WS<sub>2</sub> nanotube. In the previous study, asymmetric van der Waals layers were shown to induce shift current and generate photovoltaic effect with fixed direction<sup>33,46</sup>. The shift current is an important physical mechanism to generate the bulk photovoltaic effect with a fixed direction<sup>47</sup>. The photovoltaic effect in this work, which is programmable in both direction and magnitude by bias, should be dominated by a different mechanism. Moreover, the shift current induced anomalous photovoltaic effect would generate an open circuit photovoltage that is linearly dependent of the channel length<sup>48</sup>. However, as shown in Supplementary Fig. 24, the experimental results show that the  $V_{\text{ph}}$  is obviously independent of the channel length. Therefore, the shift current might contribute to the photocurrent in the WS<sub>2</sub> nanotube to a certain degree, the overall photovoltaic effect, which switches its direction by the external

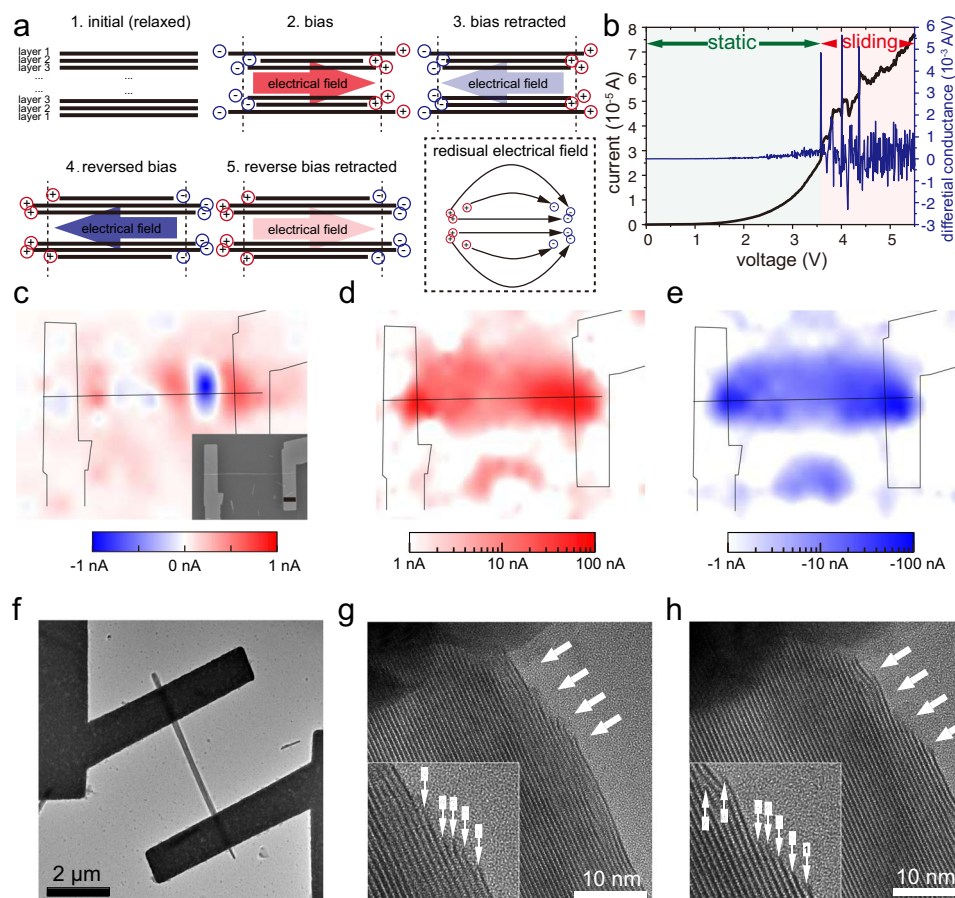


**Fig. 4 | Mechanism of the programmable photovoltaic effect.** **a** Sliding between the WS<sub>2</sub> layers, which generates residual strain and a spontaneous electric field. **b** Current and differential conductance versus voltage bias. **c** Mapped photocurrent of a WS<sub>2</sub> nanotube device before bias. The scale bar is 2  $\mu\text{m}$ . **d, e** Mapped

photocurrent of the WS<sub>2</sub> nanotube device after negative bias (**d**) and after positive bias (**e**). Note the different scales of **c–e**. The laser intensity is 1 mW. **f** A WS<sub>2</sub> nanotube device. **g, h** The layered structure of the WS<sub>2</sub> nanotube before (**g**) and after (**h**) bias.

voltage bias, should be dominated by the ferroelectric-like mechanism that switches the photovoltaic effect of WS<sub>2</sub> nanotube.

Given the superlubricity between the incommensurate van der Waals interface and the piezoelectric nature of monolayer WS<sub>2</sub> sheets<sup>23–25,30–32</sup>, we propose a mesoscopic van der Waals sliding ferroelectric effect for the WS<sub>2</sub> nanotube. As shown in Fig. 4a, Supplementary Fig. 25 and Supplementary Movies 1 and 2, the WS<sub>2</sub> nanotube consists of multiple cylindrical incommensurate layers that lack inversion symmetry, each layer has random piezoelectricity along the axial direction, depending on their chirality<sup>30,31</sup>. By applying a voltage bias, the layers of WS<sub>2</sub> with random piezoelectricity tend to extend or shrink along the axis due to the reverse piezoelectric effect<sup>32</sup>. The neighboring layers with different piezoelectricity might tend to deform in different magnitude or in opposite directions (for example, layers with positive piezoelectric coefficient tend to extend, while layers with negative piezoelectric coefficient tend to shrink). With a larger voltage bias, the shear force can exceed the low friction force between the layers and the layers will slide over to each other to extend or shrink, as shown in step 2 of Fig. 4a<sup>26–28,49–51</sup>. After the withdrawal of the bias, the layers will tend to recover from the deformation, but the friction force will prevent the full recovery, leaving the residual deformation and strain in the WS<sub>2</sub> nanotube. Due to the direct piezoelectric effect, the residual deformation will generate spontaneous electrical polarization. What is important here is that the deformed layers, whether shrunken or extended due to the opposite reverse piezoelectric coefficient, will generate electrical polarization in the same direction, and therefore generate net residual electrical polarization due to the opposite direct

piezoelectricity coefficient (see step 3). A similar analysis applies to the reverse bias (see steps 4 and 5). As such, each individual WS<sub>2</sub> nanotube is functionalized as a dedicated “nano-electro-mechanical-system”, or NEMS, plus the photovoltaic capability. The residual strain-induced piezoelectric charge concentrates at the opposite ends of the nanotube, which is similar to separated opposite point charges and generates non-volatile polarization, i.e., the van der Waals sliding ferroelectricity or sliding ferroelectricity. We note that the appropriate friction between the curved van der Waals layers is important for the preservable sliding<sup>29,52</sup>, as is shown in Supplementary Fig. 26. If there was no friction force, the sliding would not be preserved after the withdrawal of the bias, while if the friction force was too large, the interlayers are locked and sliding would hardly take place. The sliding ferroelectricity is in accordance with the experimental observations that current fluctuations dramatically increase beyond a threshold voltage, indicating the sliding of the layers inside the WS<sub>2</sub> nanotube (Fig. 4b and Supplementary Fig. 27). We also mapped the photocurrent of the WS<sub>2</sub> device before (Fig. 4c) and after negative/positive bias (Fig. 4d, e). The channel length is >10  $\mu\text{m}$ , which provides adequate spatial resolution with the laser spot size of around 1  $\mu\text{m}$ . Initially, the photocurrent is small and has varying directions along the WS<sub>2</sub> nanotube. After the positive/negative bias, we observe negative/positive photocurrent to be more intense at the end of the device, rather than at the middle of channel, which is in accordance with the simulated residual charge and voltage potential distribution, as shown in Supplementary Fig. 25 (also see discussion about the concerned Schottky contact in Supplementary Text)<sup>53</sup>. The reversion of the photocurrent is in accordance

with the Kelvin probe force microscopy (KPFM) characterized potential distribution of the WS<sub>2</sub> nanotube device channel, as shown in Supplementary Fig. 28. To further confirm the interlayer sliding of the WS<sub>2</sub> nanotube, we conducted an in situ TEM characterization. We fabricated the WS<sub>2</sub> nanotube device on a suspending SiN<sub>x</sub> film and transferred it into the TEM chamber for further characterization, as shown in Supplementary Fig. 29. By applying the positive/negative voltage of 10 V to the WS<sub>2</sub> nanotube device, the occurrence of the sliding is observed, as shown in Fig. 4f–h. As marked by the arrows, terminal edges of layers, used as visual marks in the TEM characterization, change their relative positions and provide a direct evidence for the bias induced interlayer sliding of the WS<sub>2</sub> nanotube layers.

The electric-driven sliding between van der Waals layers was also recently reported in parallelly stacked bilayer h-BN<sup>23</sup>, which generates out-of-plane ferroelectricity. However, please note that these are two fundamentally different kinds of ferroelectricity. The h-BN switches from AB to BA lattice configuration through atomic-scale sliding only in the parallel stacks and generates an interfacial out-of-plane polarization<sup>22–25</sup>. Here the cylindrical incommensurate WS<sub>2</sub> layers slide by a mesoscale norm, generate an axis parallel in-plane polarization through the reverse piezoelectric effect, and further give rise to the programmable photovoltaic effect. The immigration of defects such as intercalated oxygen ion or vacancy might also contribute to an electrostatic redistribution, however, the relatively low mobility of ions or vacancies migration is inconsistent with the observed fast current changes (see Supplementary Fig. 27) and photovoltaic effect reversion in tens of  $\mu$ s (Fig. 2a, b)<sup>54</sup>.

## Discussion

To summarize, this work reports the mesoscopic scale sliding ferroelectricity that enables a naturally embedded nano-electro-mechanical-opto-system with programmable photovoltaic effect in multiwall van der Waals WS<sub>2</sub> nanotube, and prototypes the full functional artificial vision system integrated into the WS<sub>2</sub> nanotube network. The sliding ferroelectricity, as a consequence of the mesoscopic scale superlubricity and the piezoelectricity (sliding ferroelectricity = superlubricity + piezoelectricity), is a form of spontaneous polarization that differs from the traditional ferroelectricity that arises from atomic scale ionic position shift. The mesoscopic scale sliding ferroelectricity could be further extended to other incommensurate van der Waals layers. The artificial vision system, integrated down to the material level, achieves full functions of sensing, computing, memorizing, and powering. This work provides a distinct strategy to generate ferroelectricity and programmable photovoltaic effect, and prototypes of how intelligent materials can push the integration of electronic systems towards an ultimate level.

## Methods

### Materials

Multiwall WS<sub>2</sub> nanotubes were synthesized by a two-step reaction route, when initially grown tungsten suboxide nanowhiskers are, subsequently, sulfurized into WS<sub>2</sub> nanotubes. Both reactions took place in the same reactor and under the same conditions and follow each other via a self-controlled process (a one-pot reaction). In particular, oxide nanoparticles, the precursor for this reaction, consisted of a mixture of different WO<sub>x</sub> ( $2.83 \leq x \leq 3$ ) suboxide phases and morphologies. The nanowhiskers grow via a sequence of intermediate reactions including reduction of the precursor into volatile suboxide phase (WO<sub>2.75</sub>) and its evaporation, an additional partial reduction of the vapor into WO<sub>2</sub> and condensation of the vapor mixture into 1D nanocrystals through formation of a stable W<sub>18</sub>O<sub>49</sub> suboxide phase. These suboxide nanowhiskers are converted into WS<sub>2</sub> nanotubes starting from the surface continuing inwards towards the inner core via slow diffusion-controlled

sulfurization reaction. The majority of the nanotubes range from 2 to 20  $\mu$ m in length and from 20 to 150 nm in diameter (see Supplementary Fig. 1) with a mean diameter of 70 nm.

### Devices and characterizations

WS<sub>2</sub> nanotubes were dispersed onto Si/SiO<sub>2</sub> (500 nm) wafer, and their positions were identified through optical microscopy. Electrodes were defined by electron beam lithography and electron beam evaporation of 20 nm Cr/120 nm Au or 20 nm Ti/120 nm Au followed by a lift-off process in acetone. Optical-electrical characterizations were performed with a combination of Bruker and Horiba Raman microscopes, Keithley semiconductor characterization systems, source meters, current-voltage amplifier, and oscilloscope. The 785, 633, 532, 488, 325 nm, and continuous wave lasers were implanted in the Raman microscope. The laser power was set 1 mW if not specified. For the PV-RAM array characterization, a commercial 532 nm diode-pumped solid-state laser of up to 200 mW was used to project image patterns through a customized mask, each PV-RAM was wire-bonded through a circuit control box to connect the external writing voltage, and the overall photovoltage was obtained from the outmost electrodes of the PV-RAM series. The in situ TEM sample was prepared as described in the supplementary information, and the characterization was performed with an FEI Tecnai G2 F20. The KPFM characterization was performed with a Bruker multi mode 8 AFM.

### Data availability

The data used in this study are available in the Zenodo database<sup>55</sup> with open access [<https://doi.org/10.5281/zenodo.6970428>].

### Code availability

The code that supports the findings of this study is available in Github [<https://github.com/codestonano/Zion>].

## References

1. Uyemura, J. P. *Introduction to VLSI Circuits And Systems* (2002).
2. Mack, C. A. Fifty years of Moore's law. *IEEE Trans. Semiconductor Manuf.* **24**, 202–207 (2011).
3. Tummala, R. R. & Madiseti, V. K. System on chip or system on package? *IEEE Des. Test. Computers* **16**, 48–56 (1999).
4. Tummala, R. & Swaminathan, M. *Introduction to System on Package (SOP)* (McGraw-Hill Professional Publishing, 2007).
5. Williams, M. R. A *History of Computing Technology* (Prentice-Hall, Inc., 1985).
6. Ielmini, D. & Wong, H.-S. P. In-memory computing with resistive switching devices. *Nat. Electron.* **1**, 333–343 (2018).
7. Chen, B. et al. in *2015 IEEE International Electron Devices Meeting (IEDM)*. 17.15.11–17.15.14 (IEEE, 2015).
8. Mennel, L. et al. Ultrafast machine vision with 2D material neural network image sensors. *Nature* **579**, 62–66 (2020).
9. Zhou, F. & Chai, Y. Near-sensor and in-sensor computing. *Nat. Electron.* **3**, 664–671 (2020).
10. Zhou, F. et al. Optoelectronic resistive random access memory for neuromorphic vision sensors. *Nat. Nanotechnol.* **14**, 776–782 (2019).
11. Hou, X. et al. A logic-memory transistor with the integration of visible information sensing-memory-processing. *Adv. Sci.* **7**, 2002072 (2020).
12. Zhang, Z. et al. All-in-one two-dimensional retinomorph hardware device for motion detection and recognition. *Nat. Nanotechnol.* [<https://doi.org/10.1038/s41565-021-01003-1>] (2021).
13. Kaspar, C., Ravoo, B. J., van der Wiel, W. G., Wegner, S. V. & Pernice, W. H. P. The rise of intelligent matter. *Nature* **594**, 345–355 (2021).
14. Hoffmann, M. et al. Unveiling the double-well energy landscape in a ferroelectric layer. *Nature* **565**, 464–467 (2019).

15. Valasek, J. Piezo-electric and allied phenomena in Rochelle salt. *Phys. Rev.* **17**, 475–481 (1921).
16. A century of ferroelectricity. *Nat. Mater.* **19**, 129, <https://doi.org/10.1038/s41563-020-0611-1> (2020).
17. Wu, M. 100 years of ferroelectricity. *Nat. Rev. Phys.* <https://doi.org/10.1038/s42254-021-00383-6> (2021).
18. You, L. et al. In-plane ferroelectricity in thin flakes of Van der Waals hybrid perovskite. *Adv. Mater.* **30**, 1803249 (2018).
19. Zhou, Y. et al. Out-of-plane piezoelectricity and ferroelectricity in layered  $\alpha$ - $\text{In}_2\text{Se}_3$  nanoflakes. *Nano Lett.* **17**, 5508–5513 (2017).
20. You, L. et al. Origin of giant negative piezoelectricity in a layered van der Waals ferroelectric. *Sci. Adv.* **5**, eaav3780 (2019).
21. Zheng, Z. et al. Unconventional ferroelectricity in moire heterostructures. *Nature* **588**, 71–76 (2020).
22. Yasuda, K., Wang, X., Watanabe, K., Taniguchi, T. & Jarillo-Herrero, P. Stacking-engineered ferroelectricity in bilayer boron nitride. *Science* **372**, 1458–1462 (2021).
23. Vizner Stern, M. et al. Interfacial ferroelectricity by van der Waals sliding. *Science* **372**, 1462–1466 (2021).
24. Woods, C. R. et al. Charge-polarized interfacial superlattices in marginally twisted hexagonal boron nitride. *Nat. Commun.* **12**, 347 (2021).
25. Li, L. & Wu, M. Binary compound bilayer and multilayer with vertical polarizations: two-dimensional ferroelectrics, multiferroics, and nanogenerators. *ACS Nano* **11**, 6382–6388 (2017).
26. Berman, D., Deshmukh, S. A., Sankaranarayanan, S. K. R. S., Erdemir, A. & Sumant, A. V. Macroscale superlubricity enabled by graphene nanoscroll formation. *Science* **348**, 1118 (2015).
27. Kawai, S. et al. Superlubricity of graphene nanoribbons on gold surfaces. *Science* **351**, 957 (2016).
28. Zhang, R. et al. Superlubricity in centimetres-long double-walled carbon nanotubes under ambient conditions. *Nat. Nanotechnol.* **8**, 912–916 (2013).
29. Bhushan, B., Israelachvili, J. N. & Landman, U. Nanotribology: friction, wear and lubrication at the atomic scale. *Nature* **374**, 607–616 (1995).
30. Wu, W. et al. Piezoelectricity of single-atomic-layer  $\text{MoS}_2$  for energy conversion and piezotronics. *Nature* **514**, 470–474 (2014).
31. Duerloo, K.-A. N., Ong, M. T. & Reed, E. J. Intrinsic piezoelectricity in two-dimensional materials. *J. Phys. Chem. Lett.* **3**, 2871–2876 (2012).
32. Zhu, H. et al. Observation of piezoelectricity in free-standing monolayer  $\text{MoS}_2$ . *Nat. Nanotechnol.* **10**, 151–155 (2015).
33. Zhang, Y. J. et al. Enhanced intrinsic photovoltaic effect in tungsten disulfide nanotubes. *Nature* **570**, 349–353 (2019).
34. Guo, R. et al. Non-volatile memory based on the ferroelectric photovoltaic effect. *Nat. Commun.* **4**, 1–5 (2013).
35. Choi, T., Lee, S., Choi, Y. J., Kiryukhin, V. & Cheong, S.-W. Switchable ferroelectric diode and photovoltaic effect in  $\text{BiFeO}_3$ . *Science* **324**, 63–66 (2009).
36. Setter, N. et al. Ferroelectric thin films: review of materials, properties, and applications. *J. Appl. Phys.* **100**, 051606 (2006).
37. Strukov, D. B., Snider, G. S., Stewart, D. R. & Williams, R. S. The missing memristor found. *Nature* **453**, 80–83 (2008).
38. Hus, S. M. et al. Observation of single-defect memristor in an  $\text{MoS}_2$  atomic sheet. *Nat. Nanotechnol.* **16**, 58–62 (2021).
39. Wong, H.-S. P. et al. Phase change memory. *Proc. IEEE* **98**, 2201–2227 (2010).
40. Pal, A. et al. Quantum engineered devices based on two-dimensional materials for next-generation information processing and storage. *Adv. Mater.* <https://doi.org/10.1002/adma.202109894> (2022).
41. Yang, L. et al. Efficient photovoltage multiplication in carbon nanotubes. *Nat. Photonics* **5**, 672–676 (2011).
42. Liu, J. J. et al. Aligned, high-density semiconducting carbon nanotube arrays for high-performance electronics. *Science* **368**, 850–856 (2020).
43. Bishop, M. D. et al. Fabrication of carbon nanotube field-effect transistors in commercial silicon manufacturing facilities. *Nat. Electron.* **3**, 492–501 (2020).
44. Guo, Y. F. et al. Soft-lock drawing of super-aligned carbon nanotube bundles for nanometre electrical contacts. *Nat. Nanotechnol.* **17**, 278–284 (2022).
45. Szepesvári, C. Algorithms for reinforcement learning. *Synth. Lectures Artif. Intell. Mach. Learn.* **4**, 1–103 (2010).
46. Akamatsu, T. et al. A van der Waals interface that creates in-plane polarization and a spontaneous photovoltaic effect. *Science* **372**, 68–72 (2021).
47. Kim, B., Park, N. & Kim, J. Giant bulk photovoltaic effect driven by the wall-to-wall charge shift in  $\text{WS}_2$  nanotubes. *Nat. Commun.* **13**, 3237 (2022).
48. Fridkin, V. M. in *Photoferroelectrics* (ed. Fridkin, V. M.) 85–113 (Springer Berlin Heidelberg, 1979).
49. Song, Y. et al. Robust microscale superlubricity in graphite/hexagonal boron nitride layered heterojunctions. *Nat. Mater.* **17**, 894–899 (2018).
50. Hod, O., Meyer, E., Zheng, Q. & Urbakh, M. Structural superlubricity and ultralow friction across the length scales. *Nature* **563**, 485–492 (2018).
51. Cumings, J. & Zettl, A. Low-friction nanoscale linear bearing realized from multiwall carbon nanotubes. *Science* **289**, 602–604 (2000).
52. Urbakh, M., Klafter, J., Gourdon, D. & Israelachvili, J. The nonlinear nature of friction. *Nature* **430**, 525–528 (2004).
53. Guo, Y. et al. Edge-states-induced disruption to the energy band alignment at thickness-modulated molybdenum sulfide junctions. *Adv. Electron. Mater.* **2**, 1600048 (2016).
54. Chen, Q. et al. Ultralong 1D vacancy channels for rapid atomic migration during 2D void formation in monolayer  $\text{MoS}_2$ . *ACS Nano* **12**, 7721–7730 (2018).
55. Guo, Y. et al. Mesoscopic sliding ferroelectricity enabled photovoltaic random access memory for material-level artificial vision system. <https://doi.org/10.5281/zenodo.6970428> (2022).

## Acknowledgements

We thank Prof. Lian-Mao Peng, Dr. Tingting Xu, Dr. Zhibo Liu, Dr. Duan Zhang, Dr. Xinning Song, and Dr. Pengcheng Mao for useful discussions and help with the experiments. We thank support from Natural Science Foundation of China grant 62274011, 11804024 (Y.G.), Israel Science Foundation 330/16 (A.Z.) and Israel Science Foundation 339/18 (R.T.), Beijing Institute of Technology Research Fund Program for Teli Young Fellows 3180012212208 (C.L.).

## Author contributions

Y.G. conceived and supervised this study. A.Z. synthesized the  $\text{WS}_2$  nanotube. Y.S., Z.X., S.X., J.T., M.B., Z.Q., N.Y., H.H.A., X.X., J.H., J.Y., S.W. Q.C., R.T., and Y.G. performed the experiments and analyzed the experimental data. S.X. A.Z., R.T., and Y.G. wrote the manuscript. C.L., A.Z., R.T., and Y.G. acquired funding to support this research. All authors discussed the results and contributed to writing the manuscript.

## Competing interests

Patent application has been filed by Yao Guo, Shuting Xu, Yan Sun through Beijing Institute of Technology. The remaining authors declare no competing interests.

## Additional information

**Supplementary information** The online version contains supplementary material available at <https://doi.org/10.1038/s41467-022-33118-x>.

**Correspondence** and requests for materials should be addressed to Alla Zak or Yao Guo.

**Peer review information** *Nature Communications* thanks Adilson Jesus Aparecido de Oliveira and the other, anonymous, reviewers for their contribution to the peer review of this work.

**Reprints and permission information** is available at <http://www.nature.com/reprints>

**Publisher's note** Springer Nature remains neutral with regard to jurisdictional claims in published maps and institutional affiliations.

**Open Access** This article is licensed under a Creative Commons Attribution 4.0 International License, which permits use, sharing, adaptation, distribution and reproduction in any medium or format, as long as you give appropriate credit to the original author(s) and the source, provide a link to the Creative Commons license, and indicate if changes were made. The images or other third party material in this article are included in the article's Creative Commons license, unless indicated otherwise in a credit line to the material. If material is not included in the article's Creative Commons license and your intended use is not permitted by statutory regulation or exceeds the permitted use, you will need to obtain permission directly from the copyright holder. To view a copy of this license, visit <http://creativecommons.org/licenses/by/4.0/>.

© The Author(s) 2022